crystals

MDPI

Article

Microstructural Observations, Mechanical Hierarchy, and Tribological Performance in CrFeMoV-Al$_x$ High-Entropy Alloys

Anthoula Poulia [1,*], Maria-Nikoleta Zygogianni [1], Christina Mathiou [1], Emmanuel Georgatis [1], Stavros Kiape [1], Spyros Kamnis [2] and Alexander E. Karantzalis [1]

[1] Department of Materials Science and Engineering, University of Ioannina, 45110 Ioannina, Greece; zygogiannimn@gmail.com (M.-N.Z.); christinamathiou@hotmail.com (C.M.); mgeorgat@uoi.gr (E.G.); s.kiape@uoi.gr (S.K.); akarantz@uoi.gr (A.E.K.)

[2] Department of Computer Science and Biomedical Informatics, University of Thessaly, Argonafton & Filellinon, 38221 Volos, Greece; spyros.kamnis@gmail.com

* Correspondence: apoulia@uoi.gr

Abstract

This work investigates the synthesis, thermodynamic phase stability and microstructural, mechanical and tribological behavior of the CrFeMoV alloy system and its Al-modified derivatives, CrFeMoV-Al2 and CrFeMoV-Al6, which belong to the family of high- and medium-entropy alloys. The studied systems were produced via Vacuum Arc Melting (VAM), followed by a comprehensive characterization. Thermodynamic and geometric phase-formation models were employed to predict the formation of BCC/B2 solid solutions and the potential emergence of σ-type intermetallic compounds. An ML model was also employed to further predict elemental interactions and phase evolution. These predictions were experimentally confirmed via X-ray diffraction analysis, which verified the presence of a BCC matrix in all compositions, the presence of σ-phase precipitates whose volume fraction systematically reduced with Al inclusion and the gradual increase in the B2 phase with the increase in the Al content. Scanning electron microscopy and EDX analyses uncovered noticeable dendritic segregation, with Mo and Fe enrichment in dendrite cores and in interdendritic regions, respectively. Cr, V, and Al were more uniformly distributed. Mechanical property data derived by micro hardness testing demonstrated a high hardness of 816 HV for the base alloy, ascribed to σ-phase strengthening, followed by a progressive reduction in this value to 802 HV and 756 HV in Al-containing alloys due to the attenuation of σ-phase formation and the gradual increase in the B2 phase. Dry sliding wear results unveiled a positive correlation between wear resistance and hardness, confirming the beneficial role of intermetallic strengthening. Finally, nanoindentation tests shed light on the nanoscale mechanical response, confirming the trends observed at the microscale. Overall, the combination of thermodynamic modeling and experimental analysis provide a robust framework for understanding phase stability, microstructural evolution, and mechanical performance in Al-alloyed CrFeMoV high-entropy systems, while highlighting the potential of controlled Al additions to tailor microstructure and properties.

Keywords: high-entropy alloys (HEAs); thermodynamic phase prediction; machine learning; dendritic segregation; nanoindentation; wear resistance

Check for updates

Academic Editors: Saif Haider Kayani and Byung-Joo Kim

Received: 24 December 2025
Revised: 18 January 2026
Accepted: 23 January 2026
Published: 27 January 2026

Copyright: © 2026 by the authors. Licensee MDPI, Basel, Switzerland. This article is an open access article distributed under the terms and conditions of the Creative Commons Attribution (CC BY) license.

1. Introduction

The introduction of the multi-component metallic systems concept drives a switch from alloy paradigms based on a single dominant solvent to a dynamic approach in which

configurational entropy, electronic structure, and local elastic fields mutually define phase preference, defect energetics, and eventually macroscopic performance [1]. High-entropy alloys (HEAs) epitomize this case: their near-equiatomic compositions adequately increase the configurational term in the Gibbs free energy to regularly stabilize simple crystalline lattices (BCC, FCC or their derivatives) against complex intermetallics. Still though, the existence of well-built binary and ternary bonding preferences leads to tenacious short-range order, chemical clustering, and topologically close-packed precipitates in various structures [2].

Latest critical studies point out that the modern HEA research must accordingly consider entropy as one projection among several other key factors [3,4]. For instance, valence electron concentration, atomic-size mismatch and pairwise enthalpy still remain critical points in setting which local minimum of the multi-component free-energy prospect the material will occupy [5].

Within this notional framework the CrFeMoV family holds an instructive position since it compares elements with contrasting electronic tendencies and diffusion mobilities: Mo and Cr possess strong negative mixing enthalpies that control the formation of σ-type topologically close-packed phases, whereas Fe and V tend to stabilize disordered BCC/B2 matrices and modulate ductility. Equiatomic CrFeMoV displays a dendritic microstructure in as-cast condition and arc-melted states and regularly accommodates quantifiable σ-phase fractions that firmly increase hardness, but reduce toughness. Such observations line up with focused work on Cr- and V-containing HEAs that correlate σ-formation with VEC and local pair interactions [6].

The inclusion of Al to transition-metal HEAs acts as a highly impactful chemical perturbation, since it simultaneously lowers the valence electron concentration, enlarges the average atomic volume, and unveils a high oxygen affinity. Each of these effects adjust both bulk phase equilibria and surface reactivity. Preliminary experimental evidence of Al-modified Cr- and Co-based HEAs manifest that modest Al contents can shift phase balance towards BCC/B2 ordering, refine dendritic length scales, and, in some compositions, enhance hardness and strength [7]. On the contrary, in other cases, the same Al additions tend to destabilize desirable intermetallic strengthening phases and corrosion resistance [8]. Hence, Al acts not as a simple solid-solution strengthener, but as a multi-functional alloying factor whose net effect must be perceived through integrated thermodynamic, kinetic, and electronic studies [9].

Beyond phase equilibria, the notion of local chemical order (LCO) has appeared as a pivotal microscale mechanism that reconciles the seemingly opposed considerations of both high stiffness/hardness and sluggish diffusion in several HEAs. LCO promotes spatially varying bond strengths and locally preferred atomic patterns that roughen dislocation pathways, elevate activation barriers for slip, and initiate depth- and rate-dependent mechanical responses noticeable by nanoindentation [10]. Recent theoretical and experimental evidence shows that changes in LCO, whether caused by alloying (e.g., Al additions) or by thermal/mechanical processing, produce measurable reductions in indentation modulus and alter the size and morphology of the plastic zone beneath an indenter [11]. Therefore, any comprehensive study of CrFeMoV-Al_x alloys should associate bulk thermodynamic predictions to LCO statistics and their mechanical response [12].

The FeMoVCrAl system represents a critical intersection between transition-metal and refractory high-entropy alloys, engineered primarily for extreme environments where high-temperature strength and oxidation resistance are non-negotiable. Current research has pivoted from basic phase discovery to the fine-tuning of multi-phase microstructures and the mitigation of environmental degradation.

The compositional logic of FeMoVCrAl is predicated on the high configurational entropy necessary to stabilize a body-centered cubic (BCC) matrix, yet recent studies highlight that these type of systems rarely remain a purely disordered solid solution [13]. Instead, the high atomic-size mismatch between the large Mo (1.39 Å) and smaller Cr (1.28 Å) atoms induces severe lattice distortion, which is now recognized as the primary driver for its exceptional athermal yield strength, often exceeding 1200 MPa. Advanced characterization using Atom Probe Tomography (APT) and Density Functional Theory (DFT) has recently shown that what was once thought to be a single-phase BCC often contains nanoscale B2-ordered clusters or Laves phase precipitates (Fe_2Mo-type). These secondary phases, while increasing hardness, are the subjects of intense study regarding their role in restricting dislocation mobility and promoting "sluggish diffusion" effects that enhance creep resistance up to 900 °C.

A critical review of the current state of FeMoVCrAl research reveals a significant reliance on empirical design rules (such as VEC, δ, Ω) which often fail to account for local chemical ordering [14]. While the VEC rule correctly predicts a BCC structure when VEC < 6.8, it does not account for the enthalpy-driven segregation observed in Mo-rich domains. Furthermore, much of the existing literature is limited to as-cast or homogenized states; there is a distinct lack of long-term thermomechanical fatigue (TMF) data, which is essential for aerospace certification. The "sluggish diffusion" hypothesis, a cornerstone of HEA theory, has also come under scrutiny; recent tracer diffusion experiments suggest that diffusion in FeMoVCrAl is not universally slower than in complex steels, but rather highly element-specific [15].

Research into the mechanical properties of FeMoVCrAl remains relatively limited compared with more commonly studied systems (e.g., CoCrFeMnNi) or other refractory compositions such as Mo-Nb-V, Mo-Nb-Ti-V. In general, HEAs with BCC structures show high yield and ultimate strengths at room and elevated temperatures, but often at the cost of reduced ductility at ambient conditions, a trend attributed to solid-solution strengthening and lattice-distortion effects inherent to multi-component systems. For example, alloys such as MoNbTaTiV exhibit very high hardness (~443 HV) and compressive fracture strengths in the GPa range at room temperature, highlighting the potential of HEA designs for structural applications. However, systematic tensile, fatigue, and long-term thermomechanical data for FeMoVCrAl specifically are scarce in the open literature, and most studies focus on as-cast or heat-treated microstructures rather than on detailed stress–strain behavior, fracture toughness, or high-temperature creep and fatigue performance [16]. This gap underscores the need for dedicated mechanical characterization of FeMoVCrAl under relevant service conditions to evaluate its viability for high-temperature applications.

Finally, the economic viability of these complex systems is currently constrained by significant metallurgical and financial hurdles. Specifically, the prohibitive cost of Vanadium, coupled with the processing complexities arising from the vast disparity in melting points between Aluminum (660 °C) and Molybdenum (2623 °C), limits these alloys to specialized, high-value applications rather than broad industrial adoption [17].

Based on the aforementioned aspects, the present work interrogates how incremental Al additions (2 and 6 at.%) reconfigure the CrFeMoV free-energy landscape, alter the balance between σ formation and BCC/B2 stabilization, redistribute Mo and Fe during solidification, and thereby modulate hardness, modulus, and sliding wear. The subsequent sections correlate thermodynamic criterion and ML calculations with structural observations and multi-scale mechanical measurements in order to formulate a mechanistic, quantitatively constrained narrative that links electronic structure perturbations, local chemical order dynamics, and macroscopic tribo-mechanical performance.

2. Materials and Methods

The CrFeMoV, CrFeMoV-Al2, and CrFeMoV-Al6 alloys, with specific compositions listed in Table 1, were synthesized via Vacuum Arc Melting (VAM) using high-purity elemental feedstock. Each sample was melted at least five times, followed by flipping between each melt, to promote optimal chemical homogeneity. The final shape of the samples was drops, in an ellipsoidal shape (meniscus) with dimensions around 3–4 cm in diameter, 1.5 cm in height, and a weight of 15 g.

Table 1. Actual compositions (measured by SEM-EDS elemental mapping) of the three produced alloys (CrFeMoV, CrFeMoV-Al2, and CrFeMoV-Al6) given in atomic percent (at.%), weight percent (wt.%), and the grams of each component (gr alloy) needed to make a specific total mass of the alloy.

Constituent Elements	CrFeMoV					CrFeMoV-Al2					CrFeMoV-Al6				
	at.%	wt.%	GR Alloy	Actual at.%	Actual wt.%	at.%	wt.%	GR Alloy	Actual at.%	Actual wt.%	at.%	wt.%	GR Alloy	Actual at.%	Actual wt.%
Cr	25.0	20.4	3.062	25.73	21.02	23.8	20.0	2.996	24.95	20.90	23.0	19.49	2.924	23.86	20.40
Fe	25.0	21.9	3.288	26.36	23.13	23.8	21.4	3.216	25.74	23.15	23.0	20.94	3.141	23.70	21.77
Mo	25.0	37.7	5.650	24.75	37.31	23.8	36.9	5.528	22.45	34.69	23.0	35.96	5.394	22.01	34.73
V	25.0	20.0	3.000	23.15	18.53	23.8	19.6	2.937	24.84	20.38	23.0	19.1	2.865	24.38	20.42
Al	-	-	-	-		5.0	2.18	0.327	2.01	0.87	10.0	4.496	0.674	6.05	2.69

Thermodynamic parameters and geometric factors were calculated using standard theoretical models to predict the structural tendencies, prior to synthesis. Such modeling of phase formation in the CrFeMoV-Al_x based alloys requires an integrated, quantitative assessment of the configurational, enthalpic, and geometric contributions to the Gibbs free energy, in place of a qualitative implementation of isolated norms. The configurational entropy ΔS_{mix} was determined from the ideal solution model -$R\Sigma c_i \ln c_i$ [18], while the value of ΔH_{mix} was calculated from the weighted binary interaction parameter Ω_{ij} ($\Omega = T_m \Delta S_{mix} / |\Delta H_{mix}|$ [19]. The atomic-size mismatch δ, was derived from the divergence of discrete atomic radii from the radius-weighted mean and the atomic packing factor γ compared the essential packing efficiency around the smallest and largest atoms [20]. The valence electron concentration (VEC) was computed from $\Sigma c_i VEC_i$ [21] and Senkov's k^1_{cr} model associated ΔH_{mix} with ΔH_{IM} (the enthalpy of intermetallic formation) through the critical ratio $k^1_{cr}(T) = \Delta H_{IM} / \Delta H_{mix}$ [22].

A language transformer-based machine learning model was also employed to predict phase formation. Two relative studies [23,24], demonstrate how language-model architectures can be systematically adapted for both property prediction and phase formation classification in HEAs. The earlier study [24] introduces the foundational concept of treating HEA compositions as language-like sequences processed by a BERT-style transformer. In this framework, elemental symbols and discretized thermodynamic descriptors (e.g., VEC, atomic-size mismatch, and mixing enthalpy) are custom-tokenized to preserve chemical semantics that would otherwise be lost with generic NLP tokenizers. The model employs a transfer learning architecture where the transformer is first pre-trained using masked language modeling (MLM) on a randomly generated unsupervised dataset of 1 million compositions. This step enables the model to capture thermodynamic 'grammar' and elemental interactions without reliance on experimental labels. Subsequently, fine-tuning is performed on a labeled dataset of 1184 experimental HEA compositions derived from

literature, available at https://github.com/SPS-Coatings/HEA-pre-trained-transformer (accessed on 23 December 2025), utilizing a train/validation split to optimize performance. Regarding the model output, the system generates classification probability scores (e.g., BCC: 0.82, BCC + Sec: 0.18) rather than simple binary labels. Only the higher probability label is reported.

Building directly on this architecture, the subsequent paper [23] extends the same transformer paradigm to continuous mechanical property prediction. While the earlier work emphasizes classification accuracy and ensemble strategies, the later study provides a rigorous, controlled benchmarking of transformer regression performance against established ML models, including random forests, Gaussian processes, gradient boosting, k-nearest neighbors, and decision trees. Crucially, all models are trained on identical datasets without hyperparameter optimization or data cleaning, ensuring that performance differences can be attributed to model architecture rather than pre-processing advantages. The results show that pre-trained transformers consistently outperform baseline regressors for both properties underscoring the effectiveness of transfer learning in composition-property mapping under data-scarce conditions.

Across both studies, pre-training dataset size emerges as a dominant factor governing model performance. In phase prediction, validation accuracy increases monotonically with larger unsupervised datasets, while in property regression, increasing the pre-training set from 1000 to 150,000 compositions leads to marked improvements in MSE and R2. This convergence of findings across classification and regression tasks strongly supports the notion that transformer models benefit from near-unlimited synthetic pre-training data, with computational cost rather than data availability becoming the primary constraint.

An additional unifying contribution of these works is model interpretability. Attention-weight visualizations consistently highlight chemically meaningful interactions, such as Ni-Co, Ni-Fe, and Ni-V pairs, aligning with known thermodynamic affinities, FCC stabilization mechanisms and experimental observations in CoCrFeMnNi-based systems. In the phase prediction study, attention maps and LIME-based explanations are explicitly used to guide compositional modifications that promote secondary-phase formation.

X-ray diffraction analysis was performed using Cu K_α radiation (Bruker, Billerica, MA, USA, D8 Advance) over a wide angular range to capture all reflections. SEM imaging (SEM-JEOL 6510 LV, Tokyo, Japan), equipped with backscattered electron (BSE) and energy dispersive spectroscopy (EDS) detectors (both from Oxford Instruments, Abingdon, UK) in secondary and backscattered electron modes provided insights into solidification morphology and chemical partitioning. EDX mapping quantified compositional gradients between dendritic and interdendritic regions.

Microhardness was measured using a Vickers indenter at standard loads and dwell times (Schimadzu HV-2, Shimadzu Ltd., Kyoto, Japan), while nanoindentation was conducted using a Berkovich tip at depths of 1000 and 2000 nm in two speeds (Schimadzu—DUH-211S, Shimadzu Ltd., Kyoto, Japan). Wear testing was performed under controlled ball-on-disk sliding conditions (CSM-Instruments TRIBOMETER, CSM Instruments, Needham, MA, USA), and wear tracks were further analyzed with SEM/EDX to highlight the observed wear mechanisms. The examined samples had a diameter of around 4 cm, while the testing parameters applied were a load of 5 N, and a linear velocity of 10 cm/s. The counterbody material was a steel ball, 100Cr6, with a diameter of 6 mm. The distance set for the test was 1000 m. Before each measurement, samples were weighed on a precision balance to record the initial mass and every 200 m the measurement was stopped, the sample was reweighed, any debris was collected, and the sample was repositioned in the tribometer for the next 200 m. The process was repeated on 3 samples of each composition.

3. Results

3.1. Theoretical Considerations: Phase Formation Prediction Models

The calculated parameters of the phase formation prediction models have been listed in Table 2.

Table 2. Calculated thermodynamic parameters of theoretical models, predicting the microstructure of the three produced alloys CrFeMoV, CrFeMoV-Al2, and CrFeMoV-Al6.

Thermodynamic and Geometric Parameters	CrFeMoV	CrFeMoV-Al2	CrFeMoV-Al6
VEC	6.25	6.2058	6.0487
δ	3.84	4.0934	4.5101
γ	1.10	1.1690	1.1686
T_m (K)	2248	2202	2157
ΔS_{mix} (J/mol·K)	11.520	12.1040	12.7211
ΔH_{mix} (kJ/mol)	−3.00	−3.847	−5.145
Ω	8.635	6.9266	5.3319
$k_1{}^{cr}$	2.727	3.7707	3.1327
Density (g/cm^3)	7.808	7.6823	7.4795

In all three alloys (CrFeMoV, CrFeMoV-Al2, CrFeMoV-Al6), the configurational entropy ΔS_{mix} persists abundantly high to establish a notable $-T\Delta S_{mix}$ stabilization term at solidification temperatures, thus equalize the emphatically negative ΔH_{mix} values consorted with refractory binary interactions (such as Cr-Mo, Mo-V, and V-Fe), which thermodynamically advocate the σ intermetallic phase. The value of ΔH_{mix} designates that while the enthalpic landscape drives chemical short-range ordering, its absolute value does not outpace the threshold proposed by the Guo work (-22 to + 7 kJ·mol^{-1}) [25], placing these alloys in the regime where solid-solution formation competes rather than collapses against intermetallic stability.

The geometric parameters issue further prejudicial potential. The atomic-size mismatch δ, is non-negligible considering the large size disparity between Mo and the other components, and it likewise extends with Al addition. Nonetheless, δ remains in any case under the upper maximum for single-phase BCC retention (~8.5%), stipulating that lattice distortion is adequate to impede diffusion, and thereby kinetically suppressing σ-phase coarsening. The atomic packing factor γ exhibits a similar Al-induced shift: elevation in γ moves the system away from the $\gamma > 1.175$ regime related to governing intermetallic evolution, quantitatively accordant with the experimentally detected weakening of σ-phase intensity in the XRD patterns of the Al-bearing alloys (as will be analytically presented in the following sections).

Electronic considerations further strengthen these tendencies. VEC remains below the 6.87 threshold for all compositions, foretelling stabilization of BCC structures in line with Guo's VEC map [26]. This prediction will be further validated experimentally by the persistence of BCC/B2 peaks in the X-ray analysis, in spite of the presence of σ-phase in all samples.

Thermodynamic consistency across models is further denoted by the Ω parameter which decreases with Al, considering the lower melting point of this element in respect to the refractory constituents. This reduction in Ω abates the entropic superiority at high temperature, lowering the momentum for σ-phase formation during cooling, aligning accurately with the decreased σ-phase fractions noticed.

At last, Senkov's model for the base CrFeMoV alloy is estimated to be near, but below, the dividing line separating solid-solution stability from intermetallic dominance, a hint that clarifies the coexistence of BCC and σ-phase. With Al addition, both ΔH_{mix} and ΔH_{IM} shift towards reduced values, and their ratio moves closer to the solid-solution regime, imitating a reduced enthalpic incentive for σ-phase precipitation and supporting the trend for B2 formation.

Hence, when applied holistically rather than individually, the thermodynamic (ΔH_{mix}, ΔS_{mix}, VEC, Ω, k^{cr}) and geometric (δ, γ) models establish a valid, prognostic landscape that accurately interprets the experimentally observed transition from a σ-rich microstructure in CrFeMoV alloy to progressively more stabilized BCC/B2 solid solutions upon Al inclusion.

3.2. Phase Prediction Using New ML Methods and Interpretation of Element–Element Attention Heat Maps

Table 3 summarizes the model phase predictions, while Figure 1 demonstrates how the model perceives elemental interactions.

Table 3. Phase formation ML predictions.

	CrFeMoV	CrFeMoV-Al2	CrFeMoV-Al6
Phases (ML)	BCC (1)	BCC (1) + BCC (2)	BCC (1) + BCC (2)

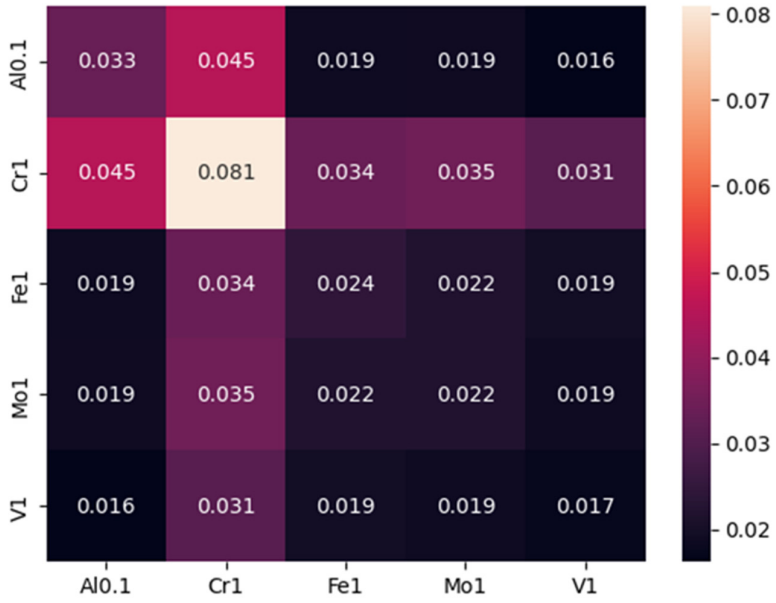


Figure 1. Elemental interactions perceived by the ML model employed in the current work.

The element–element attention heat map (Figure 1) provides a quantitative representation of how the transformer model internally couples different alloying elements when encoding the CrFeMoV-Al composition space. Numerically, the diagonal terms correspond to self-attention, reflecting how strongly an element's own representation is reinforced during encoding. In the present case, Cr exhibits the highest diagonal attention value, indicating strong internal consistency and identifying Cr as the dominant structural anchor in the learned representation. This implies that variations involving Cr exert a disproportionate influence on the model's interpretation of the alloy state. Off-diagonal terms capture pairwise interaction saliency. Moderately high values for Cr-Mo, Cr-Fe, and Cr-V indicate strong coupling among these elements. In contrast, Al-Cr interactions are elevated relative to other Al-containing pairs, while Al-V shows the lowest attention value, suggesting minimal affinity between Al and V in the learned interaction space. Collectively,

this pattern indicates selective interaction restructuring rather than uniform mixing as Al is introduced.

From a physical perspective, these attention values should not be interpreted as direct measures of any explicit thermodynamic quantity. Instead, attention reflects how strongly a change in one elemental component statistically modifies the role of another element in the model's prediction of structure or properties. As such, attention maps encode emergent, data-driven dependencies that summarize which elemental relationships are most influential for the predictive task. This makes attention-based interpretation fundamentally complementary to phase diagram calculations and experimental characterization: it highlights interaction saliency learned from data without imposing predefined physical rules, while remaining agnostic to specific mechanisms unless corroborated externally.

When interpreting the attention maps for the CrFeMoV-Al$_x$ system (Figure 2), a clear correspondence emerges. The attention maps reflect a behavior through a Cr-centered interaction network, strengthened Cr-Mo and Cr-V couplings, and persistently weak Al-V interaction saliency. The model suggests that Al-Cr attention is stronger than Al-Fe, indicating that Al preferentially interacts with the Cr-dominated lattice backbone rather than with Fe-centered environments. These patterns demonstrate that the transformer is not memorizing phase labels, but instead learning which elemental interactions co-stabilize phases, which drive phase separation, and which remain structurally inactive. The emergence of this interaction hierarchy—without explicit thermodynamic inputs—aligns with experimentally observed BCC formation pathways and established valence electron concentration and atomic-size mismatch trends in CrFeMoV-Al alloys.

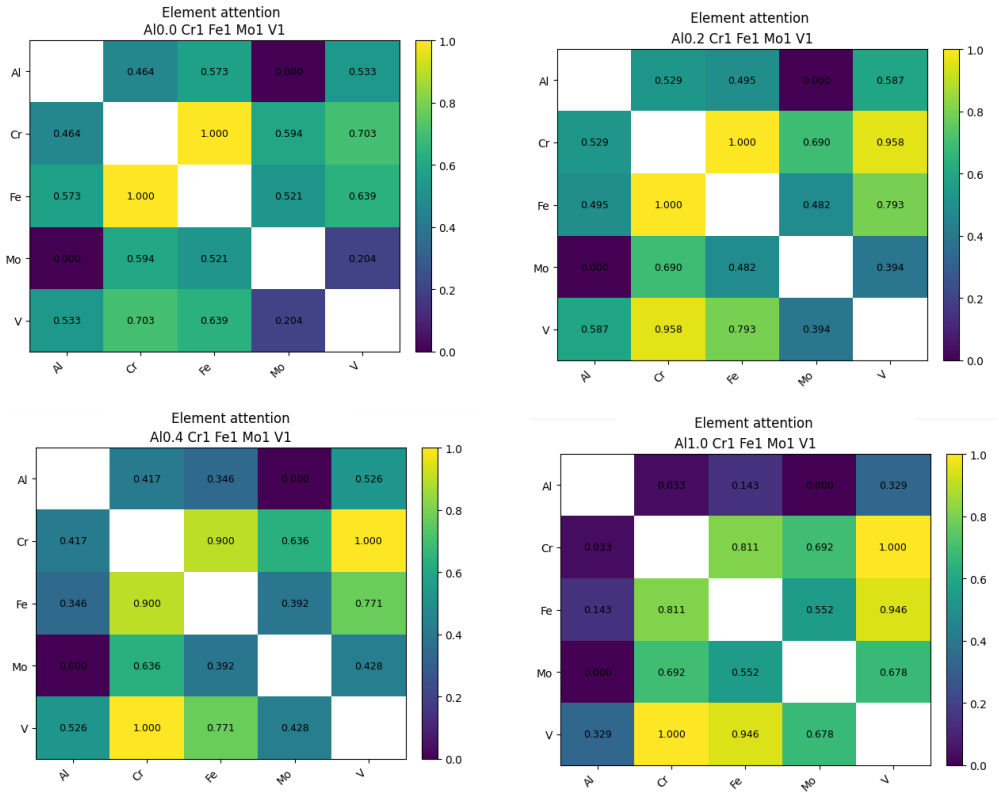


Figure 2. Evolution of elemental attention maps with increased Al content.

The base CrFeMoV alloy forms a single-phase BCC structure, while Al addition promotes the formation of a second BCC phase whose volume fraction increases with Al content and whose chemistry is enriched in V together with Cr and Mo. Aluminum stabilizes the BCC lattice overall, but destabilizes the single-phase solid solution, driving chemical partitioning rather than homogeneous mixing.

It is important at this point that the system does not predict the formation of σ phase. This behavior is technically attributed to data scarcity and class imbalance in the fine-tuning dataset. The secondary phase (Sec) represented only 41 instances (approximately 3.5%) and the BCC + Sec phases 121 instances (approximately 10%) of the total 1184 training samples, compared to dominant phases like BCC-only (32.6%) and FCC-only (29.7%). This significant imbalance limits the model's ability to learn the complex, non-linear features associated with sigma-phase formation, leading to the observed false negatives despite thermodynamic favorability. This, by no means, can be considered as a weakness of the approach as the overall process of ML is a dynamic one, which is continuously self-improved and re-adopted by the addition of new data feedback. Across the full CrFeMoV-Al_x series, the attention maps (Figure 2) show a progressive transition from a broadly distributed interaction landscape at low Al to a strongly partitioned interaction architecture at high Al (and this evolution is consistent with the experimentally reported microstructural development as Al is increased). At Al = 0, the attention matrix is comparatively less polarized and the interaction weights are more evenly distributed across element pairs, indicating that the model represents the alloy through a relatively homogeneous transition-metal interaction network. As Al increases ($0.2 \rightarrow 0.4 \rightarrow 0.6 \rightarrow 1.0$), the maps evolve toward increasingly concentrated coupling among Cr-V-Mo, accompanied by a relative suppression of cross-links from this subset to the remaining elements. In interpretability terms, the model is increasingly encoding a clustered V-Cr-Mo interaction backbone, rather than a single uniformly mixed network.

In parallel, Al's role in the attention structure is selective rather than uniformly integrative. While Al-Cr remains comparatively more salient than Al-Fe, the Al-V interaction stays persistently weak across the series, and Al-Mo remains suppressed relative to the strongest refractory–refractory couplings. This pattern indicates that increasing Al content reorganizes how the model couples the refractory elements (V, Mo) to each other more than it drives strong direct pairwise integration between Al and the V-rich sub-network. Such an attention signature denotes compositional partitioning: with increasing Al, a second BCC phase develops and grows in the volume fraction, and that phase is enriched primarily in V with additional Cr and Mo, whereas Al is not the dominant constituent of the V-rich phase chemistry and should be partly consumed, possibly through oxide formation pathways.

Taken together, the attention maps and their monotonic compositional trend provides a coherent model-based interpretation consistent with the experimental mechanism: Al acts as a compositional driver that destabilizes a more homogeneous single-phase representation and promotes a chemically differentiated, dual-network interaction structure, where V-Cr-Mo becomes increasingly tightly coupled and effectively separated in interaction space from the rest of the alloy constituents. In this reading, the transformer is not merely associating compositions with labels; rather, it is learning an interaction hierarchy in which the emergence and strengthening of a V-Cr-Mo sub-network tracks the experimentally observed evolution toward increasing phase complexity with Al addition.

To address this limitation in future models, strategies beyond simple data accumulation will be required. We propose the integration of physics-informed loss functions, where thermodynamic constraints (e.g., CALPHAD-derived enthalpy thresholds) explicitly penalize predictions that violate phase stability rules. Furthermore, implementing active learning loops to selectively target and label experimental compositions in underrepresented phase regions could systematically correct this imbalance, enhancing sensitivity to complex intermetallics.

3.3. XRD: Competing Thermodynamic Drivers and the Evolution of Phase Stability

The diffractograms of the investigated systems plotted in Figure 3 disclose a BCC matrix whose stability hardly abates with the incremental incorporation of Al, despite the simultaneous presence and depletion of σ-phase reflections. The persistence of BCC peaks across all three compositions denotes that the configurational entropy remains adequately high to counterbalance the negative mixing enthalpies associated with Cr-Mo and Cr-V pairs, both of which strongly endorse topologically close-packed (TCP) structures, such as the σ-phase.

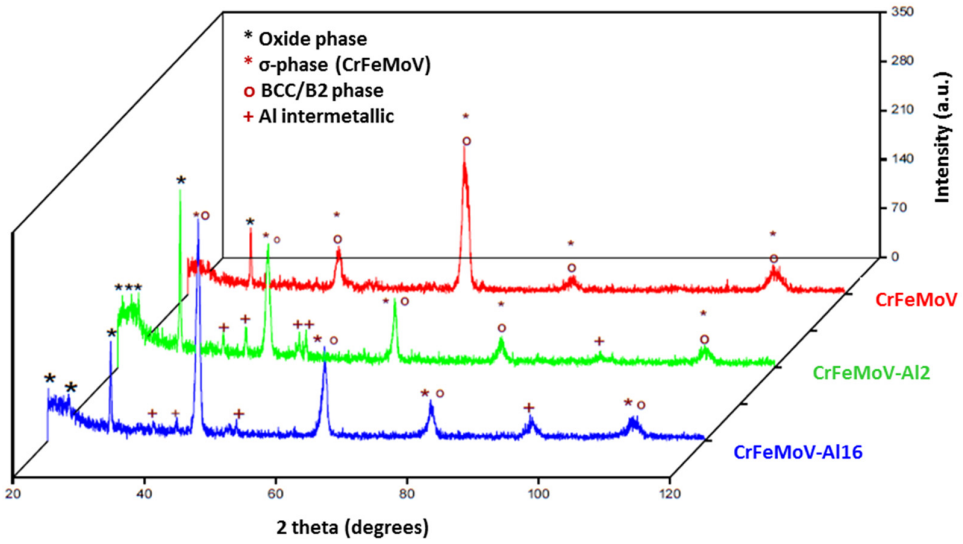


Figure 3. X-ray diffraction (XRD) patterns for the synthesized CrFeMoV, CrFeMoV-Al2, and CrFeMoV-Al6 alloys.

The systematic importance lies not only in the proximity of σ-phase, but in its regularized destabilization as Al increases. The attenuation of σ-phase intensity is not solely a dilution outcome; it is the straight result of a shift in the free-energy landscape. Al addition decreases VEC (see data of Table 1), which modifies the Fermi surface–Brillouin zone interactions that stabilize the σ-phase [27]. Coincidentally, Al addition increases δ and therefore the strain energy penalty for solidifying an ordered σ-lattice, whose site-specific occupancy is prone to atomic-size contrast. These two perturbations—electronic and elastic—unite to boist the σ-phase Gibbs free energy, in relation to the BCC solution.

The simultaneous genesis of weak superlattice reflections implies that Al does not solely suppress σ-phase, but leads the BCC lattice towards partially ordered states reminiscent of B2-like chemical short-range order. This is in line with the known tendency of Al-containing HEAs to display B2/BCC duality at intermediate enthalpies [28]. Finally, the presence of low-angle oxide peaks is thermodynamically foreseeable; Al's exceptionally negative affinity to oxygen guarantees that surface oxidation is kinetically favored, even under minimal exposure [29]. This last observation concerning the arising of double BCC/B2 phase combination, comes in absolute agreement with the findings and the predictions of the ML approach, previously discussed.

Hence, the XRD patterns reflect a competition between configurational entropy, electronic stabilization, atomic-size-driven strain effects, and site-specific ordering tendencies. Al acts as a perturbing agent that relocated the balance toward a chemically disordered, but electronically stabilized BCC matrix, while steadily suppressing intermetallic complexity.

3.4. Microstructure: Interplay of Solidification Path, Solute Partitioning, and Diffusion Dynamics

Figure 4 displays the dendritic microstructure of the three alloys, which is formed during solidification through a partitioning regime. The spacing between these dendritic arms is significantly influenced by the addition of Al. The base alloy (Figure 4a,b) exhibits a clear dendritic morphology with noticeable segregation. It presents the coarsest dendritic structure, controlled by Mo-rich cores nucleating early. The addition of 2 at.% Al (Figure 4c,d) leads to a compression of dendrite arm spacing. This refinement is attributed to Al's high diffusivity, which disrupts the thermal gradient and advances constitutional supercooling ahead of the solidification front. With 6 at.% Al (Figure 4e,f), the microstructure becomes more homogenized. Al effectively disrupts the Mo-dominated clustering tendency, leading to a reduction in the thermodynamic penalty for homogenization and the eventual elimination of distinct Mo segregation.

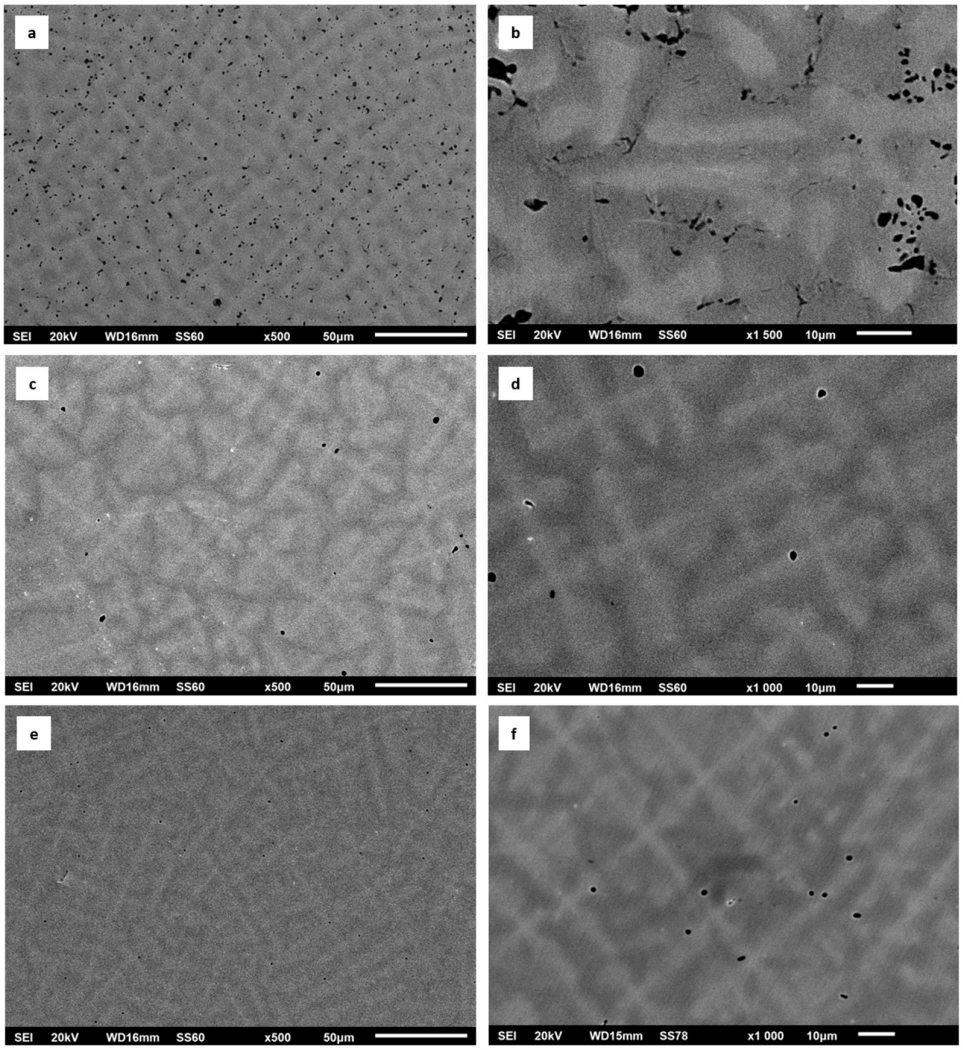


Figure 4. Scanning electron microscopy (SEM) images summarizing the microstructural outcomes of the three synthesized alloys: (**a**,**b**) CrFeMoV; (**c**,**d**) CrFeMoV-Al2; and (**e**,**f**) CrFeMoV-Al6.

In addition, the dendritic microstructure observed in the alloys synthesized declares that solidification proceeds through a strongly partitioning regime controlled by the differential diffusion coefficients and liquidus slopes of the constituent elements. EDX point and line-scan analysis (Figure 5) show that Mo, possessing the lowest diffusivity and highest melting point among the constituent elements, segregates into the dendritic cores due to the

strong Mo-Cr and Mo-V interactions that raise the local solidus, therefore causing Mo-rich regions to nucleate earlier in the solidification sequence.

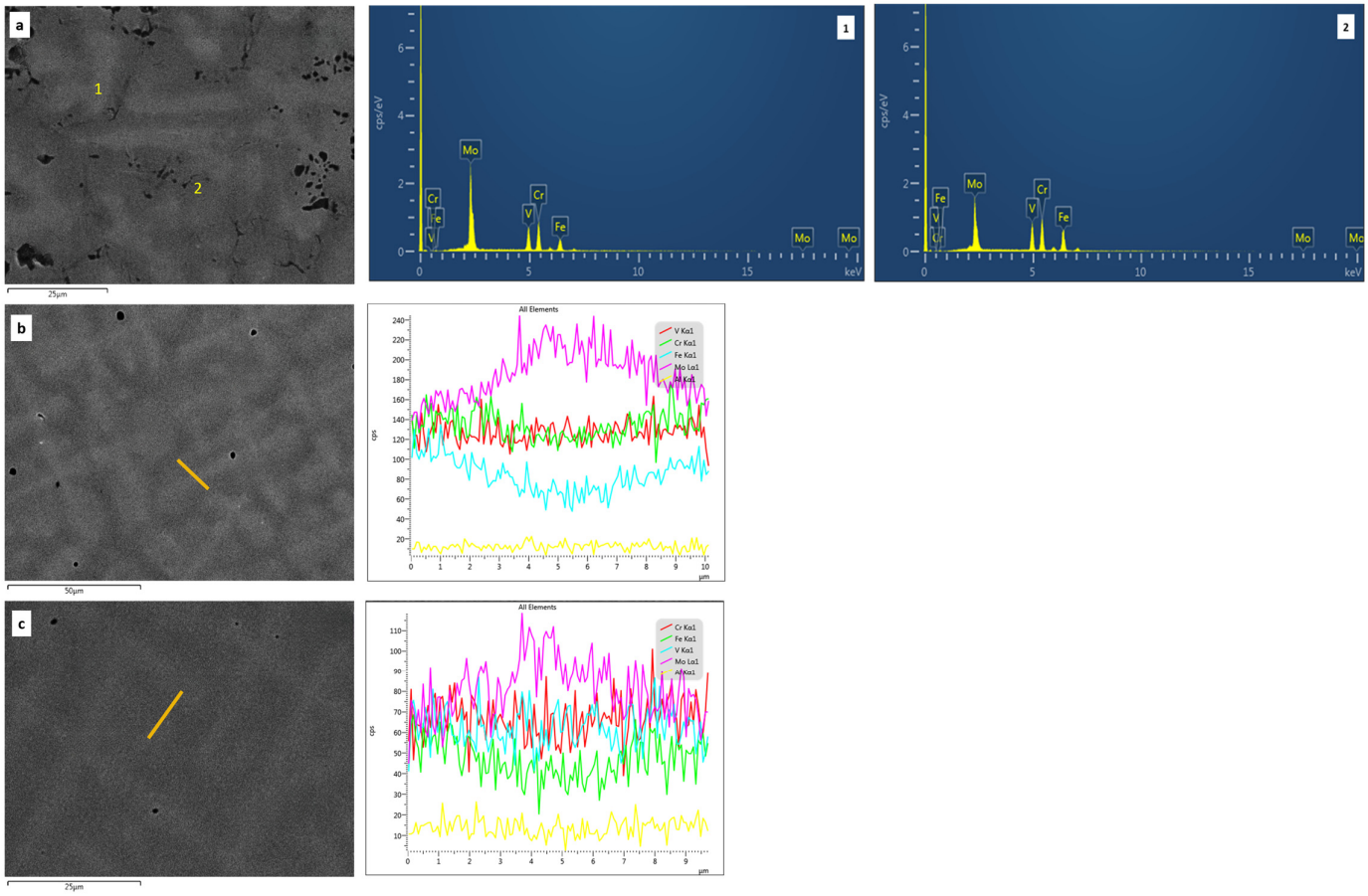


Figure 5. Point and line-scan EDX analysis for the (**a**) CrFeMoV, (**b**) CrFeMoV-Al2, and (**c**) CrFeMoV-Al6 alloys.

Fe, with higher diffusivity and a lower liquidus, is expelled into the interdendritic liquid, accumulating preferentially in the terminal stages of solidification. The resulting microstructure is not a straightforward dendrite/interdendrite dichotomy, but a chemically polarized microstructure, shaped by the coaction of unequal solute mobilities, liquidus curvature, and constitutional supercooling dynamics.

The addition of Al (Figure 5b) perturbs this segregation motif by adjusting the respective mobilities in both the solid and liquid. Al's high diffusivity in Fe-based systems disrupts the thermal gradient ahead of the solidification front, advancing constitutional supercooling and compressing dendrite arm spacing [30]. The refinement detected in the Al2 alloy is thus a kinetic feedback to modified solute redistribution.

In the case of Al6 alloy (Figure 5c), the elimination of Mo segregation is particularly revealing: it points out that the increased configurational entropy and reduced σ-phase driving force, diminish the thermodynamic penalty for homogenization. Al effectively disrupts the Mo-dominated clustering tendency by increasing the free-energy cost of forming highly ordered Mo-rich σ-precursors. This behavior reflects a competition between Mo-driven ordering and Al-driven disorder, with Al gradually prevailing at higher concentrations.

To summarize the aforementioned findings it can be stated that the observed microstructure records a thermodynamic transition from chemically polarized solidification to a more homogenized, entropy-stabilized one, modulated by diffusional asymmetries and the progressive destabilization of cluster precursors.

3.5. Hardness: Mechanistic Breakdown of Strengthening Contributions

The hardness decrease (Figure 6) across the alloys when adding Al is not merely a correlational observation, but a quantitative manifestation of the competing strengthening mechanisms. In the base CrFeMoV alloy, hardness originates from three principal sources:

(i) Solid-solution strengthening, amended by substantial lattice distortion from the large atomic radius differences among Mo, V, and Fe elements;
(ii) Precipitation strengthening, considering the presence of the σ-phase, whose complex tetragonal lattice imparts significant resistance to shearing and dislocation bypass phenomena [31];
(iii) Cluster strengthening, from Mo-enriched dendritic regions that behave as stiff microstructural domains with high local elastic moduli.

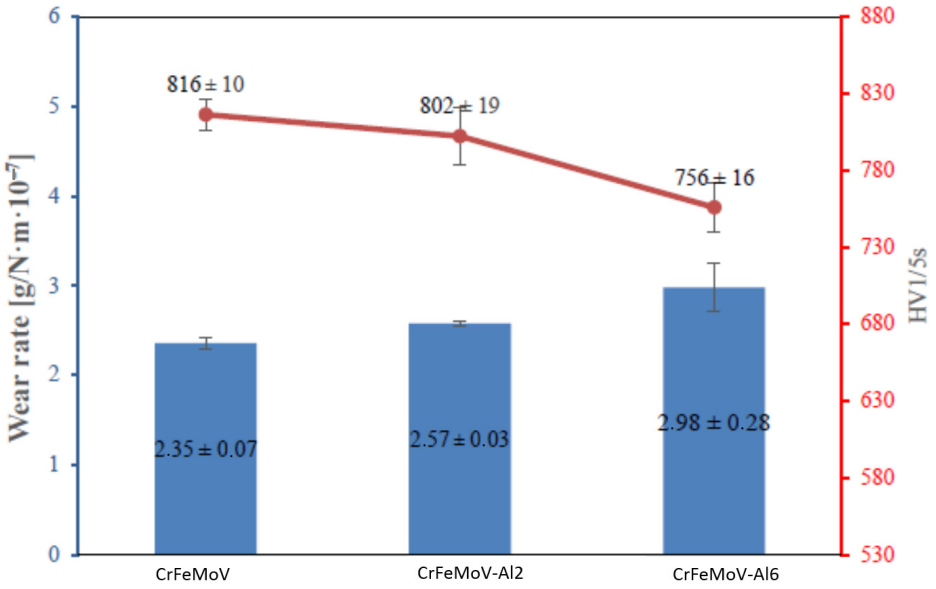


Figure 6. Trend of the wear rate vs. hardness, HV, for the synthesized alloys.

On the other hand, when Al is introduced in the system, each of these strengthening factors is behaving in a distinct manner. Al reduces the σ-phase fraction not only volumetrically, but also mechanistically via decreasing site occupancy contrast in the Cr-Mo sublattice, thereby diminishing the internal stress fields that hinder dislocation flow [32]. Likewise, the replacement of Mo-rich regions by Al-modified BCC matrix regions (associated with the rise in the B2 phase) brings down the modulus contrast that shapes internal barriers to slip transmission.

Al also alters Peierls stress by modifying the electron density around slip planes [33]. BCC slip is particularly prone to electronic filling [34] and Al-driven VEC drop when its at.% raises (see values in Table 1), decreasing the lattice friction stress [35]. This electronic weakening competes against the modest lattice-distortion strengthening introduced by the inclusion of relatively small Al atoms into the large-atom Cr-Mo-V environment.

The subsequent hardness profile reflects a net softening, conquered by the disintegrate of σ-phase strengthening and the drop of Mo-driven modulus gradients, with lattice distortion incapable of compensating for these compositional shifts.

3.6. Correlation Between Microhardness and Grain Size-Evolution

The microhardness response of the CrFeMoV-Al_x alloys exhibits a monotonic decrease with increasing Al content, from 816 HV for the base CrFeMoV alloy to 802 HV for CrFeMoV-Al2 and further to 756 HV for CrFeMoV-Al6. When these hardness values are analyzed

in conjunction with the microstructural observations, it becomes evident that grain-size refinement alone cannot account for the observed mechanical softening.

SEM analysis demonstrates that Al additions promote dendrite arm refinement and compress the characteristic solidification length scales, particularly in the Al2 alloy, which would normally be expected to enhance hardness through a Hall–Petch-type mechanism. However, the experimental trend clearly contradicts this expectation, indicating that grain-boundary strengthening plays a secondary role compared to phase and chemical effects in this system.

The dominant factor governing hardness reduction is the progressive suppression of the σ-phase with Al addition, as confirmed by XRD and microstructural analysis.

In the base CrFeMoV alloy, the σ-phase forms a mechanically stiff, topologically close-packed reinforcement embedded within the BCC matrix, contributing significantly to hardness via precipitation strengthening and dislocation pinning. Although grain sizes are relatively coarser in this alloy, the σ-phase contribution overwhelms any potential Hall–Petch softening associated with larger grains. As Al is introduced, σ-phase volume fraction diminishes systematically, reducing the density of strong barriers to dislocation motion. This reduction in intermetallic strengthening offsets—and ultimately surpasses—the beneficial effect of grain refinement.

Furthermore, Al alters solute partitioning and reduces Mo segregation, leading to a more chemically homogenized BCC matrix at higher Al contents. This homogenization lowers internal modulus gradients between dendritic and interdendritic regions, which otherwise act as effective obstacles to plastic flow. Consequently, even though Al additions refine microstructural features, the simultaneous loss of σ-phase strengthening and Mo-rich cluster hardening leads to a net decrease in hardness. The microhardness results therefore reflect a transition from a phase-dominated strengthening regime (σ-phase-controlled) in CrFeMoVCr to a grain-size-insensitive, chemically softened regime in CrFeMoV-Al6.

In summary, the combined analysis of microhardness and grain-size evolution reveals that, in the CrFeMoV-Al_x system, grain refinement is not the controlling factor for hardness. Instead, the mechanical response is governed by the competition between σ-phase precipitation strengthening and Al-induced chemical and electronic softening of the BCC matrix. This finding highlights a critical limitation of applying conventional Hall–Petch arguments to high-entropy alloys where phase stability and local chemical order dominate mechanical behavior.

3.7. Wear Mechanisms: Merging Tribological Behavior with Microstructure and Electronic Structure

The tribological response of the examined alloys is a direct mechanical expression of the microstructural hierarchy. A typical relationship in materials science is observed in Figure 6 where hardness is often directly proportional to wear resistance for abrasive or adhesive wear mechanisms. The addition of Al from 0 at.% to 6 at.% in the CrFeMoV system has a detrimental effect on the wear resistance improvement.

Regarding the evaluation of the wear tracks morphology and corresponding EDX analysis, in the CrFeMoV alloy (Figures 7a and 8a), the high hardness and retained σ-phase produce a wear track with minimal plowing, where the σ-phase acts as an in situ ceramic network. The metallic matrix between σ-domains is too confined to undergo significant plasticity, leading to a predominantly micro-abrasive mechanism with negligible adhesive contribution.

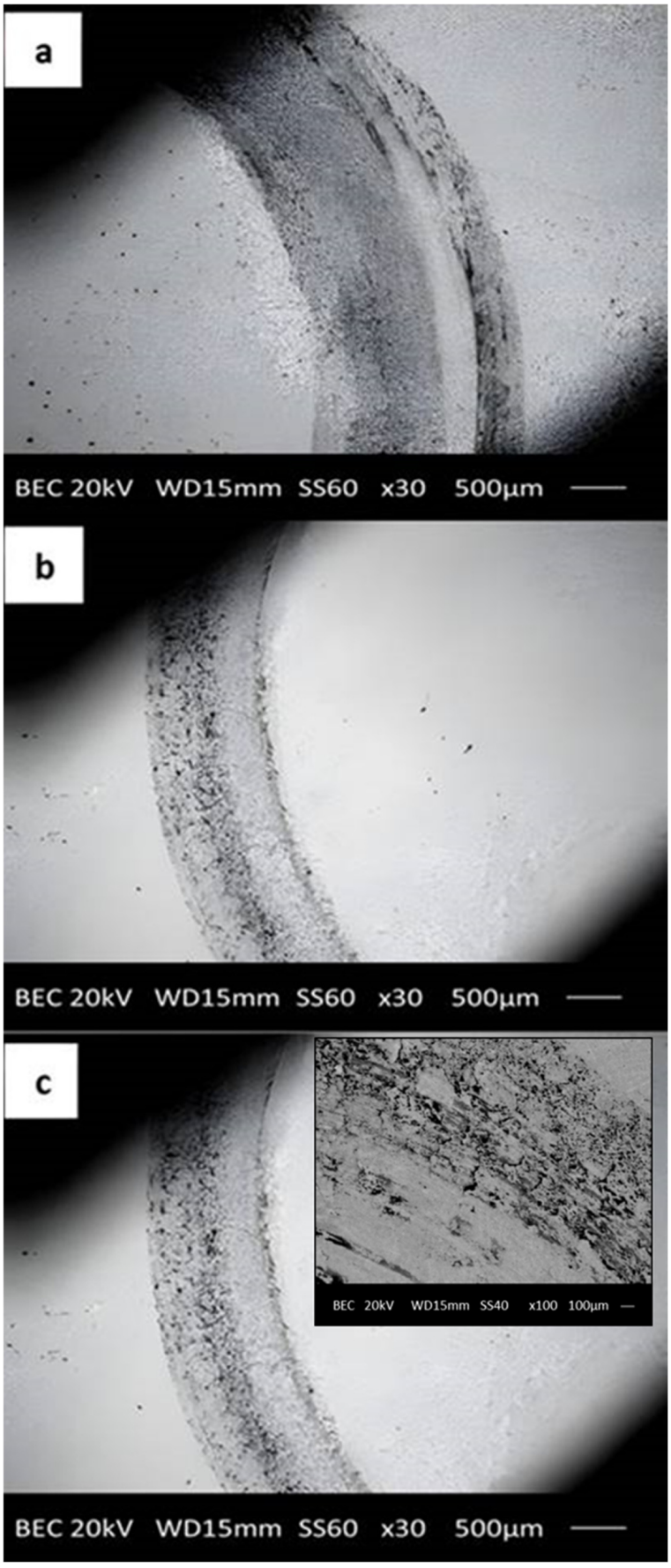


Figure 7. Wear track morphology of the (**a**) CrFeMoV, (**b**) CrFeMoV-Al6, and (**c**) CrFeMoV-Al6 alloys.

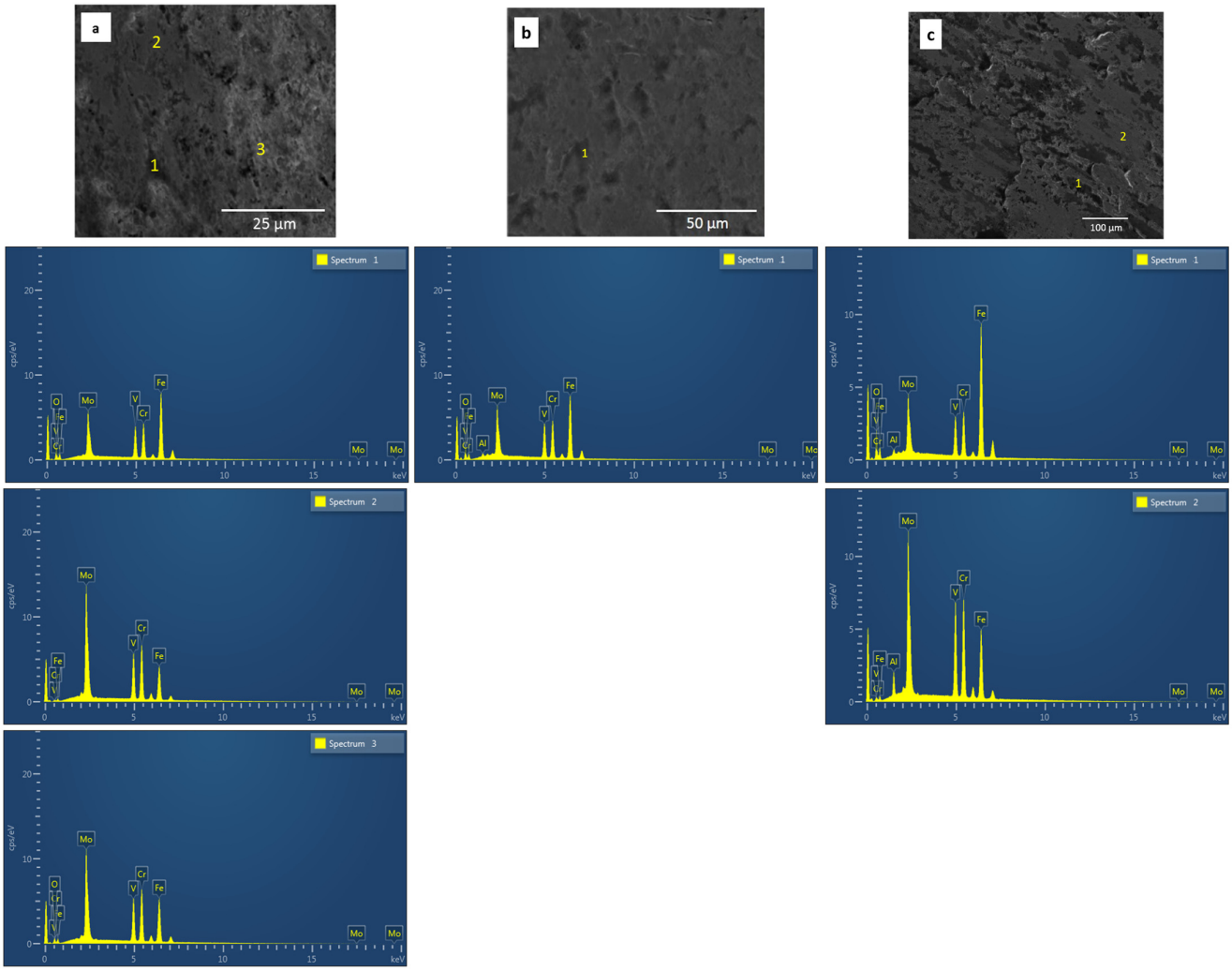


Figure 8. EDX analysis on the wear tracks of the (**a**) CrFeMoV, (**b**) CrFeMoV-Al2, and (**c**) CrFeMoV-Al6 alloys.

As Al is added in the original alloy (Figures 7b and 8b), the progressive disappearance of σ-phase and the formation of B2 phase, remove this in situ skeleton, transferring the load-bearing responsibility to the BCC/B2 matrix. Therefore, the BCC/B2 matrix, now chemically diluted by Al, experiences a reduced shear modulus and diminished dislocation mean free path barrier. Consequently, the wear track of the Al2 alloy exhibits more pronounced plastic deformation signs, while the dominant wear mechanism shifts towards abrasion, complemented by micro-cracking of the weakened interdendritic regions.

In the Al6 alloy (Figures 7c and 8c), the tribological behavior becomes more complex. The enlarged presence of Al oxides, the refined microstructure, and the reduced intrinsic hardness promote adhesive interactions between the alloy surface and the counterface material. The synergy of these effects produces a mixed wear regime in which delamination, third-body abrasion, and adhesion all coexist. The scale of material removal becomes governed not merely by mechanical hardness, but by the electronic and chemical instabilities introduced by high Al concentrations, which modify surface bonding and accelerate oxide-assisted wear.

Thus, wear behavior reflects a correlated structural–chemical degradation pathway, tightly tied to the dissolution of σ-phase architecture and the accompanying electronic weakening of the BCC/B2 matrix.

3.8. Nanoindentation: Local Chemical Order and Strain-Field and Depth-Dependent Softening

Nanoindentation testing was employed to probe the local mechanical response of the CrFeMoV, CrFeMoV-Al2, and CrFeMoV-Al6 alloys at the nanoscale, under controlled indentation depths and loading rates. The extracted indentation elastic modulus ($E_{(it)}$), hardness (HV), and indentation creep parameter ($n_{(it)}$) are summarized in Table 4.

Table 4. Nanoindentation results for the CrFeMoV, CrFeMoV-Al2, and CrFeMoV-Al6 alloys measured at two maximum indentation depths (1000 and 2000 nm) and different loading rates (13.3 and 2.2 nm·s^{-1}). E_{it} is the indentation elastic modulus obtained from the Oliver–Pharr method, HV is the indentation hardness, and n_{it} is the indentation creep (time-dependent deformation) parameter expressed as a percentage. Indentation speed refers to the loading rate and is given in nm·s^{-1}.

1000 nm						
	E_{it} (N/mm^2)		**HV**		**n_{it} (%)**	
Alloy	**Speed 13.3 nm·s^{-1}**	**Speed 2.2 nm·s^{-1}**	**Speed 13.3 nm·s^{-1}**	**Speed 2.2 nm·s^{-1}**	**Speed 13.3 nm·s^{-1}**	**Speed 2.2 nm·s^{-1}**
CrFeMoV	271,500.0	280,740.0	810	751	24.1	21.3
CrFeMoV-Al2	234,380.0	232,280.0	760	731	25.2	24.0
CrFeMoV-Al6	228,420.0	233,160	725	730	23.9	21.7
2000 nm						
	E_{it} (N/mm^2)		**HV**		**n_{it} (%)**	
Alloy	**Speed 13.3 nm·s^{-1}**		**Speed 13.3 nm·s^{-1}**		**Speed 13.3 nm·s^{-1}**	
CrFeMoV	268,820.0		786		23.4	
CrFeMoV-Al2	228,280.0		756		24.4	
CrFeMoV-Al6	195,900.0		789		28.5	

At a maximum indentation depth of 1000 nm, the base CrFeMoV alloy exhibits the highest elastic modulus, with $E_{(it)}$ values exceeding 270 GPa, reflecting the presence of stiff Mo- and Cr-rich regions and the contribution of the σ-phase. In contrast, both Al-containing alloys display systematically lower modulus values, indicating a progressive reduction in local stiffness with increasing Al content. This trend is consistent with the suppression of σ-phase strengthening and the dilution of strong transition-metal bonding within the BCC/B2 matrix.

A clear dependence on indentation loading rate is observed at 1000 nm. Lower loading rates (2.2 nm·s^{-1}) generally yield reduced $E_{(it)}$ and hardness values compared to higher rates (13.3 nm·s^{-1}), particularly in the Al-bearing alloys. This behavior suggests the activation of time-dependent deformation mechanisms, where slower loading allows local atomic rearrangements and chemical relaxations within the chemically complex lattice. The effect is more pronounced in Al-rich compositions, indicating enhanced susceptibility to rate-sensitive deformation as local chemical order is disrupted.

When the indentation depth increases to 2000 nm, a further reduction in elastic modulus is recorded for all alloys. This depth-dependent softening reflects the larger probed volume beneath the indenter, which increasingly incorporates chemically heterogeneous regions, including softer Fe- and Al-enriched zones. The effect is especially evident in the CrFeMoV-Al6 alloy, where $E_{(it)}$ decreases to approximately 196 GPa, highlighting the homogenization of stiffness and the attenuation of cluster-driven reinforcement mechanisms at larger length scales.

The indentation creep parameter ($n_{(it)}$) shows a moderate increase with Al content and indentation depth, indicating an enhanced time-dependent response in the Al-modified

alloys. This trend is consistent with a reduction in lattice friction stress and increased atomic mobility associated with Al addition, which facilitates localized stress-assisted atomic shuffling during indentation.

A possible theoretical mechanism describing these features could state that Al disrupts Mo-driven cluster formation by penalizing the formation of tightly bonded Cr-Mo environments. As LCO decreases, the matrix becomes more elastically compliant. Al-containing regions also possess lower stiffness due to weaker metallic bonding in Al-diluted environments [36]. As indentation depth increases, the sampling volume becomes increasingly dominated by these compliant regions, accelerating the modulus drop.

The rate dependence observed at lower indentation speeds further strengthens this interpretation. Slow deformation allows LCO rearrangements–essentially nano-scale chemical relaxations–to occur under the indenter. These relaxations reduce local stiffness [37] by enabling atoms to diffuse or shuffle toward lower-energy configurations, particularly in Al-rich chemical clusters. The resulting softening is not plastic in the conventional sense, but a quasi-viscoelastic response of a structurally frustrated multi-component lattice [38].

Overall, the observed depth- and rate-dependent variations in elastic modulus indirectly suggest the presence of local chemical heterogeneities. The reduction in stiffness with Al addition could be linked with the proposed disruption of Mo-driven local chemical order (LCO) statistics, as Al modifies the configurational energy topology of the alloy.

4. Discussion

The collective behavior of the CrFeMoV-Al_x system demonstrates that the mechanical and tribological performance of these alloys cannot be interpreted solely through isolated microstructural observations. Instead, the emerging property gradients arise from a complex thermodynamic–kinetic coupling in which Al acts not as a simple additive, but as a systematic perturbation to the configurational, electronic, and elastic landscape of the alloy.

The progressive suppression of the σ-phase with increasing Al content, along with a dual BCC/B2 appearance, is the most significant structural transformation and can be understood as a shift in the balance between entropic stabilization and enthalpic ordering. In the base alloy, the σ-phase exists because the enthalpic gain from forming Mo-Cr and Mo-V bond networks outweighs the configurational entropy loss associated with the formation of a topologically close-packed lattice. When Al is substituted into the system, two linked mechanisms work against σ-phase formation: first, Al lowers the VEC, which disrupts the electronic stabilization of the σ-lattice by weakening its characteristic pseudogap–Fermi level alignment [39] and, second, Al increases atomic-size mismatch and therefore amplifies strain energy penalties associated with the formation of site-specific, distortion-sensitive σ configurations. The combined effect of these mechanisms leads to a thermodynamic destabilization of the σ-phase and a shift in the system towards a chemically disordered BCC/B2 environment, despite the retained enthalpic driving forces between transition metals.

The microstructural consequences of this thermodynamic shift manifest in the redistribution of Mo. As σ-phase becomes less favorable, the strong Mo-Cr interactions do not disappear; rather, they transition from long-range-ordered structures to short-range clustering within the BCC/B2 matrix. These clusters are dynamically regulated by diffusion kinetics and local entropic gradients, creating a metastable chemical landscape in which the competition between cluster coalescence and entropy-driven dissolution governs the local elastic and plastic behavior [40]. The depth-dependent modulus reduction observed through nanoindentation provides direct mechanical evidence of this internal chemical competition. The deeper the indentation, the larger the volume over which the indenter integrates the heterogeneous stiffness distribution created by these clusters and local chemical fluctuations.

Simultaneously, Al introduces a new set of electronic and mechanical perturbations. Al has a significantly lower electron density than the transition metals it replaces, which reduces the BCC bonding strength by lowering the density of d-electron states near the Fermi level [41]. This fact shifts the alloy from a strongly metallic-bond-dominated regime towards a mixed metallic–covalent tendency, in which the weakened electron density reduces dislocation friction stress and enhances local lattice compliance.

The wear behavior of the Al6 alloy clearly reflects this transition: instead of a σ-stabilized hard skeleton constraining plasticity, the load-bearing matrix becomes soft enough to permit subsurface delamination and adhesive bridging with the counterface [42]. The presence of Al-derived oxides accelerates this process by acting as abrasive third bodies and by providing weakly bonded surface films that fracture under shear [43]. Thus, the wear behavior is not simply a hardness-controlled phenomenon, but a multi-scale interaction between chemical bonding, phase transformation, and oxide-intervened surface reactions.

Finally, the observed trends in hardness and modulus cannot be understood without considering the statistical mechanics of local chemical order. In multi-principal-element alloys, LCO stabilizes energy minimums that differ from those of long-range-ordered intermetallics [10]. These minimums act as local attractors for atomic configurations, generating clusters with high internal bonding coherence, but limited growth potential due to entropy barriers. Al disrupts these minima by altering local enthalpies and reducing the differential bonding preferences among elements. This causes a decrease in the magnitude and persistence of LCO and consequently reduces local stiffness [44].

The sensitivity of modulus to indentation rate—particularly evident in Al6—further indicates that LCO rearrangements are activated processes whose kinetics are accessible under the stresses imposed by nanoindentation [45]. These rearrangements lower the effective modulus through time-dependent relaxation phenomena analogous to microviscoelastic behavior, though originating from atomic shuffling rather than classical polymeric chain mobility.

It should be noted that while the nanoindentation trends—specifically the depth-dependent softening and rate-dependent modulus shifts—provide a compelling mechanical signature of LCO, these findings remain indirect inferences. The current study lacks direct atomic-scale mapping of these clusters. To validate the proposed LCO dynamics and their evolution with Al content, future experimental work utilizing high-resolution characterization techniques, such as Atom Probe Tomography (APT) or Transmission Electron Microscopy (TEM) with energy-dispersive X-ray spectroscopy (EDS) at the atomic scale, is required.

The tribological observations integrate seamlessly with this view. In CrFeMoV, strong LCO and σ-phase stabilizations restrict atomic mobility and produce a wear surface that deforms elastically with minimal subsurface shear localization.

In contrast, in Al-bearing alloys, the collapse of these stabilizing mechanisms increases the free volume available for atomic rearrangement during sliding, enhancing frictional heating, and accelerating surface softening [46]. This creates a feedback loop: atomic mobility increases wear-induced damage, and wear-induced damage further increases atomic mobility [47]. The progressive broadening of the wear track in Al6 is thus a signature of a mechanically induced chemical disordering process, in which tribological action enhances the migration of Al-rich clusters and the fracturing of oxide-rich surface layers.

The consistent convergence of microhardness, nanoindentation, and wear behavior suggests that the defining characteristic of the CrFeMoV-Al system is not the presence or absence of the σ-phase, but rather the modulation of chemical stiffness gradients. These gradients—reflecting spatial variations in bonding strength, cluster size, elemental mobility,

and electron density—govern the partitioning of stress, the activation of slip systems, and the resistance to localized shear [48]. The addition of Al decreases these gradients and thereby homogenizes the mechanical field, but at the cost of reducing the high-stiffness, high-modulus domains that impart wear resistance and high hardness to the base alloy.

To conclude, Al operates as a disordering agent that shifts the alloy from a heterogeneous, cluster-reinforced mechanical architecture to a more homogeneous, but mechanically weaker state. The result is a transition from a structure dominated by energetically deep, stiff Mo-Cr clusters to one governed by shallow, easily perturbed Al-Fe enriched configurations. It is this transition—not merely the loss of the σ-phase—that fundamentally controls the mechanical and tribological performance.

5. Conclusions

The CrFeMoV alloy system undergoes a profound mechanistic transformation as Al is incrementally introduced. Al acts simultaneously as an entropic stabilizer, an electronic destabilizer of σ-phase, and a local modulator of atomic-size mismatch, generating a cascade of structural and mechanical consequences. The suppression of the σ-phase and the establishment of a dual BCC/B2 combination is not a trivial dilution effect, but a thermodynamically driven reconfiguration of the energy landscape rooted in changes to VEC, strain energy, and site occupancy preferences.

Microstructurally, these thermodynamic shifts manifest in reduced Mo segregation, refinement of dendritic structures, and ultimately in the collapse of cluster-driven stiffening mechanisms, that define the base alloy.

The mechanical consequences of this collapse appear in the softening trend observed in both microhardness and nanoindentation values. The depth- and rate-dependent modulus reductions highlight the central role of local chemical order and its progressive destabilization with increasing Al content. The tribological response integrates these effects. The wear transition from predominantly abrasive in the base alloy transforms to a mixed adhesive–abrasive type in Al-bearing alloys. This behavior is a direct outcome of the weakening of cluster domains and a result of the increasing electronic and elastic compliance of the matrix.

From a theoretical standpoint, the CrFeMoV-Al system exemplifies the sensitivity of high-entropy alloys to subtle perturbations in configurational and electronic balance. The system provides a clear case study in how alloying elements influence not only discrete phases, but also the emergent mechanical architecture that arises from complex chemical interactions and multi-scale ordering phenomena. The results demonstrate that alloy strength, stiffness, and wear resistance depend less on gross composition and more on the underlying hierarchical chemical coherence—a coherence that Al progressively erodes.

To conclude, the findings of this work provide a clear roadmap for tailoring the mechanical and tribological performance of CrFeMoV-Al HEAs. The core design principle identified is the Al-driven phase transition from a hard, intermetallic-strengthened system to a more compliant, solid-solution-stabilized matrix. For applications requiring high wear resistance, low or zero Al content is preferred. In the base CrFeMoV alloy, the presence of the σ-phase acts as an in situ ceramic-like skeleton that effectively hinders abrasive plowing and maintains high hardness (816 HV). This strengthening is further supported by Mo-rich clusters that create stiff microscale domains. Conversely, Al acts as a "toughening agent" by systematically destabilizing the brittle σ-phase. Incremental Al additions (2 to 6 at.%) shift the alloy toward a BCC/B2 duplex structure, reducing the volume fraction of the hard intermetallic precipitates. This transition leads to a progressive reduction in hardness and elastic modulus, indicating a more compliant matrix capable of greater plastic

deformation—a critical requirement for enhancing fracture toughness in otherwise brittle refractory-based systems.

By precisely controlling the Al concentration, designers can move between a high-hardness, wear-resistant regime (dominated by σ-phase and local chemical order) and a tougher, more ductile regime (dominated by stabilized BCC/B2 solid solutions). This provides a mechanistic framework for developing HEAs for specific industrial environments, such as high-load sliding contacts (low Al) versus structural components requiring impact resistance (high Al).

Author Contributions: Conceptualization, A.E.K. and E.G.; Methodology, M.-N.Z., C.M., S.K. (Stavros Kiape) and S.K. (Spyros Kamnis); Formal Analysis, M.-N.Z., C.M., S.K. (Stavros Kiape) and S.K. (Spyros Kamnis); Investigation, M.-N.Z., C.M., S.K. (Stavros Kiape) and S.K. (Spyros Kamnis); Writing—Original Draft Preparation, A.P., A.E.K. and S.K. (Spyros Kamnis); Writing—Review & Editing, A.P., A.E.K. and S.K. (Spyros Kamnis); Visualization, A.E.K. and E.G.; Supervision, A.E.K. All authors have read and agreed to the published version of the manuscript.

Funding: This research received no external funding.

Data Availability Statement: The original contributions presented in this study are included in the article. Further inquiries can be directed to the corresponding author.

Conflicts of Interest: The authors declare no conflicts of interest.

References

1. Łach, Ł. Phase Stability and Transitions in High-Entropy Alloys: Insights from Lattice Gas Models, Computational Simulations, and Experimental Validation. *Entropy* **2025**, *27*, 464. [CrossRef]
2. Li, J.; Sun, J.; Liu, J.; Sun, X. The Precipitation and Effect of Topologically Close-Packed Phases in Ni-Based Single Crystal Superalloys. *J. Mater. Sci. Technol.* **2024**, *173*, 149–169. [CrossRef]
3. Kumar, A.; Mukhopadhyay, N.K.; Yadav, T.P. Recent Progresses on High Entropy Alloy Development Using Machine Learning: A Review. *Comput. Mater. Today* **2025**, *8*, 100038. [CrossRef]
4. Pickering, E.J.; Jones, N.G. High-Entropy Alloys: A Critical Assessment of Their Founding Principles and Future Prospects. *Int. Mater. Rev.* **2016**, *61*, 183–202. [CrossRef]
5. Krishna, S.A.; Noble, N.; Radhika, N.; Saleh, B. Comprehensive Review on Advances in High Entropy Alloys: Fabrication and Surface Modification Methods, Properties, Applications, and Future Prospects. *J. Manuf. Process.* **2024**, *109*, 583–606. [CrossRef]
6. Saikumaran, A.; Jaiganesh; Ghosh, C.; Mythili, R.; Sornadurai, D.; Subramanian, N.; Jaya, S.M.; Saibaba, S. Experimental and Theoretical Study of Microstructural Characteristics and Phase Stability in Equiatomic CrFeMoV Alloy. *Mater. Charact.* **2019**, *154*, 449–457. [CrossRef]
7. Yang, H.; Tan, Y.; Qiao, J.; Hawk, J.A.; Zhang, Y.; Gao, M.; Liaw, P.K. Optimize the Mechanical Properties of $Al_{0.6}$CoCrFeNi High-Entropy Alloys by Thermo-Mechanical Processing. *Metals* **2022**, *12*, 178. [CrossRef]
8. Samoilova, O.; Pratskova, S.; Shaburova, N.; Moghaddam, A.O.; Lezhnev, S.; Panin, E.; Trofimov, E. Effect of Al Content on the Microstructure, Microhardness and Corrosion Resistance of Al_xCoCrFeNi$Mo_{0.5}$ High-Entropy Alloys. *J. Chem. Technol. Met.* **2025**, *60*, 1091–1098. [CrossRef]
9. Raza, A.; Ryu, H.J.; Hong, S.H. Strength Enhancement and Density Reduction by the Addition of Al in CrFeMoV Based High-Entropy Alloy Fabricated through Powder Metallurgy. *Mater. Des.* **2018**, *157*, 97–104.
10. Dasari, S.; Sharma, A.; Jiang, C.; Gwalani, B.; Lin, W.C.; Lo, K.C.; Gorsse, S.; Yeh, A.C.; Srinivasan, S.G.; Banerjee, R. Exceptional Enhancement of Mechanical Properties in High-Entropy Alloys via Thermodynamically Guided Local Chemical Ordering. *Proc. Natl. Acad. Sci. USA* **2023**, *120*, 2211787120.
11. Ren, M.; Han, F.; Zhu, X.; Peng, Y.; Zu, Y.; Liu, P.; Feng, A. Nanoscale Indentation-Induced Crystal Plasticity in CrCoNi Medium-Entropy Alloys Containing Short-Range Order. *Materials* **2024**, *17*, 5932.
12. Guo, S.; Wang, M.; Wang, Q.; Sui, S.; Kayani, S.H.; Seol, J.B.; Zhu, P.; Guo, A.; Lin, X.; Huang, W. The Influence of Chemical Short-Range Order on the Nanoindentation Properties of High-Entropy Alloys Prepared via Laser Powder Bed Fusion. *Mater. Charact.* **2024**, *207*, 113560.
13. Feng, R.; Liaw, P.K.; Gao, M.C.; Widom, M. First-Principles Prediction of High-Entropy-Alloy Stability. *npj Comput. Mater.* **2017**, *3*, 50. [CrossRef]

14. Miracle, D.B.; Senkov, O.N. A Critical Review of High Entropy Alloys and Related Concepts. *Acta Mater.* **2017**, *122*, 448–511. [CrossRef]
15. Divinski, S.V.; Pokoev, A.; Esakkiraja, N.; Paul, A. A Mystery of "Sluggish Diffusion" in High-Entropy Alloys: The Truth or a Myth? *Diffus. Found.* **2018**, *17*, 69–104.
16. Wang, Y.; Li, F.; Li, Y.; Li, J.; Chen, H.; Bai, Y. Effects of Ultrasonic Surface Rolling Process on Microstructure and Mechanical Properties of Metastable $Fe_{50}Mn_{30}Co_{10}Cr_{10}$ High-Entropy Alloy Fabricated by Laser Directed Energy Deposition. *J. Mater. Res. Technol.* **2025**, *39*, 26–46.
17. Senkov, O.; Wilks, G.; Miracle, D.; Chuang, C.; Liaw, P. Refractory high-entropy alloys. *Intermetallics* **2010**, *18*, 1758–1765. [CrossRef]
18. Zhang, Y.; Zhou, Y.J.; Lin, J.P.; Chen, G.L.; Liaw, P.K. Solid Solution Phase Formation Rules for Multi-Component Alloys. *Adv. Eng. Mater.* **2008**, *10*, 534–538. [CrossRef]
19. Zhang, Y.; Yang, X.; Liaw, P.K. Alloy Design and Properties Optimization of High-Entropy Alloys. *JOM* **2012**, *64*, 830–838. [CrossRef]
20. Wang, Z.; Huang, Y.; Yang, Y.; Wang, J.; Liu, C.T. Atomic-Size Effect and Solid Solubility of Multicomponent Alloys. *Scr. Mater.* **2015**, *94*, 28–31. [CrossRef]
21. Guo, S.; Hu, Q.; Ng, C.; Liu, C.T. More than Entropy in High Entropy Alloys: Forming Solid Solutions or Amorphous Phase. *Intermetallics* **2013**, *41*, 96–103. [CrossRef]
22. Senkov, O.; Miracle, D.B. A New Thermodynamic Parameter to Predict Formation of Solid Solution or Intermetallic Phases in High Entropy Alloys. *J. Alloys Compd.* **2016**, *658*, 603–607.
23. Kamnis, S.; Delibasis, K. High Entropy Alloy Property Predictions Using a Transformer-based Language Model. *Sci. Rep.* **2025**, *15*, 11861. [CrossRef] [PubMed]
24. Kamnis, S. Introducing Pre-trained Transformers for High Entropy Alloy Informatics. *Mater. Lett.* **2024**, *358*, 135871. [CrossRef]
25. Guo, S.; Liu, C.T. Phase Stability in High Entropy Alloys: Formation of Solid-Solution Phase or Amorphous Phase. *Prog. Nat. Sci. Mater. Int.* **2011**, *21*, 433–446.
26. Guo, S.; Ng, C.; Lu, J.; Liu, C.T. Effect of Valence Electron Concentration on Stability of Fcc or Bcc Phase in High Entropy Alloys. *J. Appl. Phys.* **2011**, *109*, 103505. [CrossRef]
27. Tsai, M.H.; Tsai, K.Y.; Tsai, C.W.; Lee, C.; Juan, C.C.; Yeh, J.W. Criterion for σ Phase Formation in Cr- and V-Containing High-Entropy Alloys. *Mater. Res. Lett.* **2013**, *1*, 207–212.
28. Lass, E.A. On the Thermodynamics and Phase Transformation Pathways in BCC-B2 Refractory Compositionally Complex Superalloys. *Metall. Mater. Trans. A* **2022**, *53*, 4481–4498.
29. Jeurgens, L.P.H.; Sloof, W.G.; Tichelaar, F.D.; Mittemeijer, E.J. Growth Kinetics and Mechanisms of Aluminum-Oxide Films Formed by Thermal Oxidation of Aluminum. *J. Appl. Phys.* **2002**, *92*, 1649–1656. [CrossRef]
30. Yan, J.; Liu, T.; Wang, M.; Sun, J.; Dong, S.; Zhao, L.; Wang, Q. Constitutional Supercooling and Corresponding Microstructure Transition Triggered by High Magnetic Field Gradient During Directional Solidification of Al-Fe Eutectic Alloy. *Mater. Charact.* **2022**, *188*, 111920. [CrossRef]
31. Zou, S.; Dong, C.; Tan, X.; Liang, Z.; Bao, W.; He, B.; Lu, W. Mitigating Embrittlement of Sigma Phase in Dual-Phase High-Entropy Alloys Through Heterostructure Design. *Int. J. Plast.* **2025**, *287*, 104272. [CrossRef]
32. Laube, S.; Chen, H.; Kauffmann, A.; Schellert, S.; Müller, F.; Gorr, B.; Müller, J.; Butz, B.; Christ, H.J.; Heilmaier, M. Controlling Crystallographic Ordering in Mo–Cr–Ti–Al High Entropy Alloys to Enhance Ductility. *J. Alloys Compd.* **2020**, *823*, 153805. [CrossRef]
33. Kamimura, Y.; Edagawa, K.; Takeuchi, S. Experimental Evaluation of the Peierls Stresses in a Variety of Crystals and Their Relation to the Crystal Structure. *Acta Mater.* **2013**, *61*, 294–309. [CrossRef]
34. Borges, P.P.P.O.; Ritchie, R.O.; Asta, M. Electronic Descriptors for Dislocation Deformation Behavior and Intrinsic Ductility in Bcc High-Entropy Alloys. *Sci. Adv.* **2024**, *10*, 7670. [CrossRef] [PubMed]
35. Sahu, K.L.; Venkatesh, K.; Kumar, A.; Jaiswal, A.; Verma, J.; Yerra, L.; Bos, P.S.C. Effect of Aluminum Addition on Microstructure, Mechanical Properties, and Wear Behavior of MoNbTiV Refractory High-Entropy Alloys. *Adv. Eng. Mater.* **2025**, *27*, 202501702. [CrossRef]
36. Xin, H.; Yang, J.; Mao, J.; Chen, Q.; Yang, J.; Zhang, W.; Ning, Z.; Teng, C.; Ma, C.; Wu, L.; et al. Effect of Al Concentration on Microstructure and Properties of AlNbTiZr Medium-Entropy Alloy Coatings. *Materials* **2021**, *14*, 7661. [CrossRef] [PubMed]
37. Tian, Y.; Fang, Q.; Li, J. Molecular Dynamics Simulations for Nanoindentation Response of Nanotwinned FeNiCrCoCu High Entropy Alloy. *Nanotechnology* **2020**, *31*, 465701. [CrossRef] [PubMed]
38. Abusabir, A.; Khan, M.A.; Asif, M.; Khan, K.A. Effect of Architected Structural Members on the Viscoelastic Response of 3D Printed Simple Cubic Lattice Structures. *Polymers* **2022**, *14*, 618. [CrossRef]
39. Ravindran, P.; Asokamani, R. Correlation Between Electronic Structure, Mechanical Properties and Phase Stability in Intermetallic Compounds. *Bull. Mater. Sci.* **1997**, *20*, 613–622. [CrossRef]

40. Zhang, J.Y.; He, Q.F.; Li, J.; Yang, Y. Chemical Fluctuation Enabling Strength-Plasticity Synergy in Metastable Single-Phase High Entropy Alloy Film with Gigapascal Yield Strength. *Int. J. Plast.* **2021**, *139*, 102951.
41. Pant, D.; Aidhy, D.S. Electronic Density of States as the Descriptor of Elastic Bond Strength, Ductility, and Local Lattice Distortion in BCC Refractory Alloys. *Mater. Des.* **2025**, *253*, 113885. [CrossRef]
42. Liu, H.; Wang, R.; Wang, Q.; Chen, P.; Yang, H.; Hao, J.; Sun, S.; Liu, X. Tribology Behavior in Laser Cladded Dual-Phase $Al_xCoCrFeNiMn_{(1-x)}$ High Entropy Alloys Influenced by Hierarchical Interface Architecture. *Surf. Coat. Technol.* **2023**, *471*, 129895. [CrossRef]
43. Wilson, S.; Alpas, A.T. Thermal Effects on Mild Wear Transitions in Dry Sliding of an Aluminum Alloy. *Wear* **1999**, *225–229*, 440–449. [CrossRef]
44. Chen, M.; Yang, X.; Zhao, X.; Wen, C.; Huang, H. Effect of Al Content and Local Chemical Order on the Stacking Fault Energy in Ti-V-Zr-Nb-Al High-Entropy Alloys Based on First Principles. *Materials* **2025**, *18*, 2053. [CrossRef]
45. Sun, Y.; Huo, Y.; Yu, W.; Yan, Z.; Wang, Z.; Li, Z.; Wang, Z.; Chen, H.; Jiang, A.; Wang, X. Microstructure and Nanoindentation Creep Behavior of NiAlCrFeMo High-Entropy Alloy. *J. Alloys Compd.* **2025**, *1020*, 179330. [CrossRef]
46. Chuang, M.H.; Tsai, M.H.; Wang, W.R.; Lin, S.J.; Yeh, J.W. Microstructure and Wear Behavior of $Al_xCo_{1.5}CrFeNi_{1.5}Ti_y$ High-Entropy Alloys. *Acta Mater.* **2021**, *59*, 6308–6317. [CrossRef]
47. Zhai, W.; Bai, L.; Zhou, R.; Fan, X.; Kang, G.; Liu, Y.; Zhou, K. Recent Progress on Wear-Resistant Materials: Designs, Properties, and Applications. *Adv. Sci.* **2021**, *8*, 2003739. [CrossRef] [PubMed]
48. Ma, E.; Wu, X. Tailoring Heterogeneities in High-Entropy Alloys to Promote Strength–Ductility Synergy. *Nat. Commun.* **2019**, *10*, 5623. [CrossRef]

Disclaimer/Publisher's Note: The statements, opinions and data contained in all publications are solely those of the individual author(s) and contributor(s) and not of MDPI and/or the editor(s). MDPI and/or the editor(s) disclaim responsibility for any injury to people or property resulting from any ideas, methods, instructions or products referred to in the content.